Schweizerischer Erdbebendienst
Service Sismologique Suisse
Servizio Sismico Svizzero
Swiss Seismological Service

ETH
Eidgenössische Technische Hochschule Zürich
Swiss Federal Institute of Technology Zurich

SITE CHARACTERIZATION REPORT

SENGL: Engelberg (OW)

Francesco Panzera, Paolo Bergamo, Donat Fäh

Last Modification: 20th May, 2020

Schweizerischer Erdbebendienst (SED)
Service Sismologique Suisse
Servizio Sismico Svizzero
Servizi da Terratrembels Svizzer

ETH Zürich
Sonneggstrasse 5
8092 Zürich
Schweiz
francesco.panzera@sed.ethz.ch

Contents

Summary

The SSMNet station SENGL was installed 27.09.2018 in the territory of the municipality of Engelberg (OW) about 500 m North-East of the city centre. From a geological point of view, the station is located on gravel ("Bachschutt") on the North-Western of the Engelberger Aa river. Active seismic measurements, as well as two single-station ambient vibration measurement surveys, were performed to characterize the subsurface structure beneath the station. The site is characterized by a low amplitude fundamental frequency peak at about 1.5 Hz, which can be related to an interface between rock formations, well beyond the investigation depth reached by our measurements (which is approximately 30-40 m). Moreover, the general HVSR amplitude trend at the station close to SENGL tends to increase its amplitude gradually at higher frequency, showing a broadband distribution of peaks, which can usually be associated to alternating layers with different velocities. The estimated V_{S30} value is 493 m/s, which classifies the site as C type in SIA261 (SIA, 2014) and B type soil according to Eurocode 8 (CEN, 2004).

1 Introduction

The station SENGL is part of the Swiss Strong Motion Network (SSMNet). The station has been installed on 27.09.2018 in the framework of the second phase of the Swiss Strong Motion Network (SSMNet) renewal project (Fig. 1). In order to better characterize the subsurface at the station, we performed an active seismic survey and single station measurements of ambient vibrations.
The site is of interest because it is located in central Switzerland at the border between the Molasse basin and the Helvetic nappes. Its geographical location improves the network coverage of the area.
The measurement campaign was carried out on 27 September 2019 in order to characterize the soil column in terms of fundamental frequency and shear wave velocity.

Figure 1: Map showing the location of the strong motion station (red circle) in Engelberg. © 2019 swisstopo (JD100042)

2 Geological setting

A geological map of the surroundings of the site in Engelberg is shown in Fig. 2 The seismic station SENGL is located on the western side of a conoid deposit (gravel), extending from North to South. This conoid is bordered in the North by landslide deposit, to ENE by moraine deposits, in the West by fine-grained scree and to the South by alluvial deposits of the Engelberger Aa river.

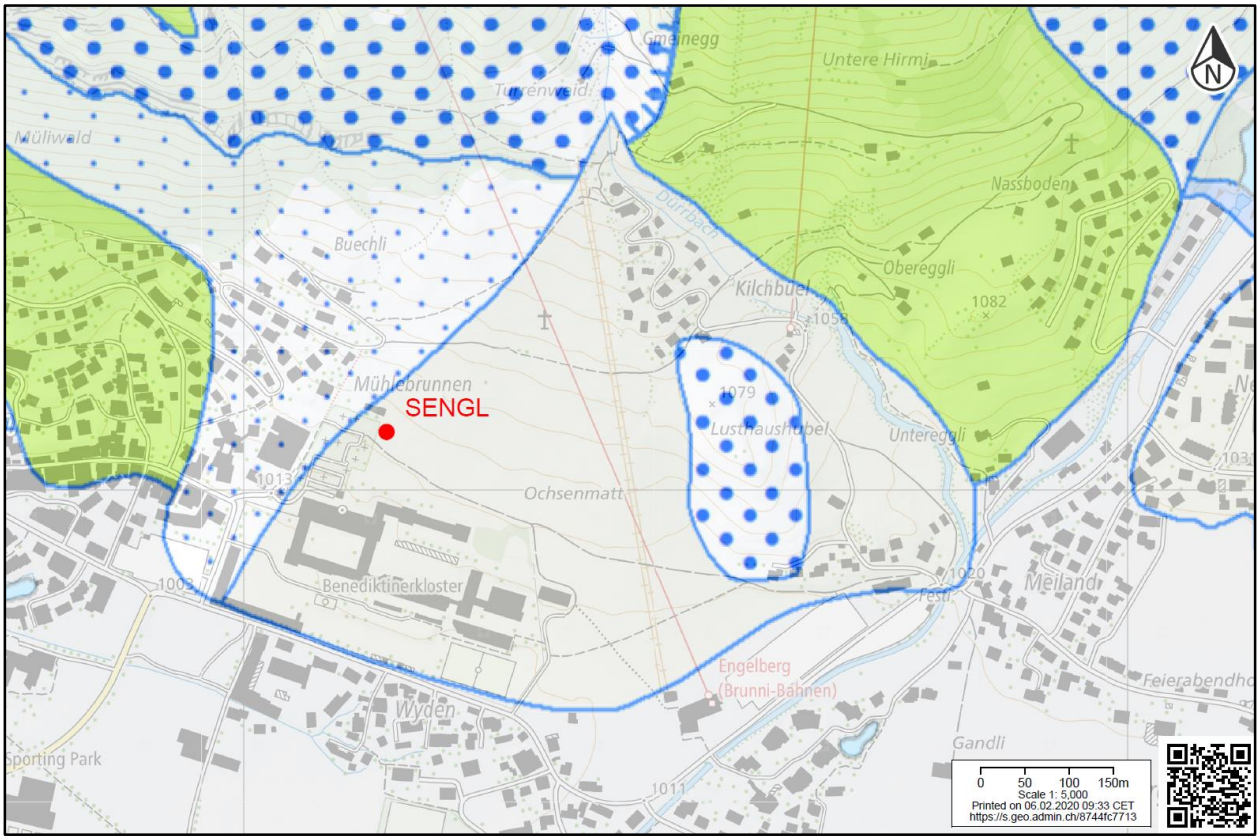

Figure 2: Geological map of the SENGL seismic station area identified by a red circle. Light green =moraine; gray area = alluvial sediments; white with large dots = landslide deposit*; white with small dots = fine-grained scree; light yellow = conoid deposit. © 2019 swisstopo (JD100042)*

3 Active seismic measurements

The active seismic line was deployed close to SENGL (about 100 m far), along a WNW-ESE direction (Figure 3). For the sake of a comprehensive subsurface characterization, multichannel analysis of surface waves (MASW; Park et al., 1999) and P-wave refraction (Redpath, 1973) surveys were conducted.

3.1 Equipment

We used three sets of 8 three-component geophones (4.5 Hz corner frequency). Each geophone set was connected to a Geode datalogger; the three Geodes were coupled for time synchronization. The seismic source was a 5-kg sledgehammer, hitting a flat metal plate at seven source locations (yellow stars in Figure 3), as well as a wedge-shaped plate for Love wave excitation at the two shot points outside the geophone line. This plate is an isosceles right triangle: the hypotenuse is placed on the ground, and coupled to it with spikes penetrating the soil. The catheti are oriented orthogonally to the geophone spread, and alternately hit with the hammer.

The synchronization between the traces recorded by the geophones and the seismic source was ensured by a trigger device fastened to the hammer handle.

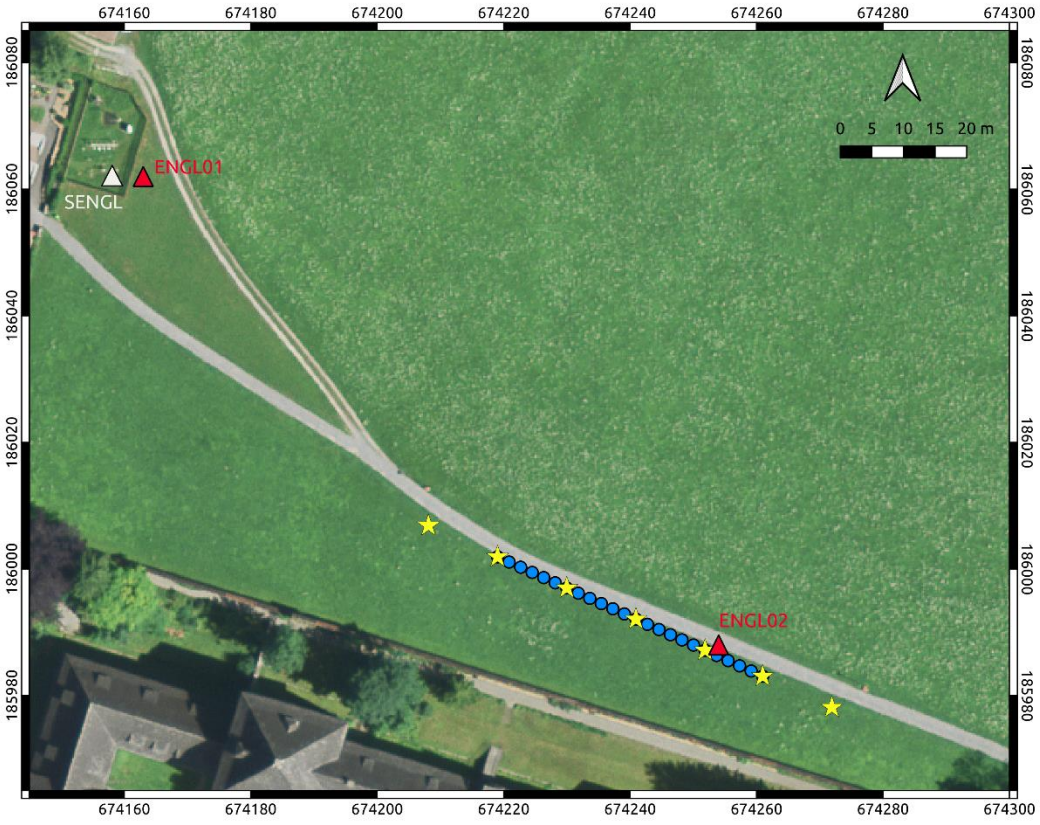

Figure 3: Map representing the position of the targeted station (SENGL, white triangle), of the active seismic line (yellow stars – sources, blue circles - geophones) and of the noise recording sensors (reds triangles).

3.2 Geometry of the acquisition array

The seismic line was constituted by 24 three-component receivers aligned at regular intervals of 2 m, for a total length of 46 m. The geophones were laid on the soil with metal spikes ensuring a firm coupling with the ground.

As earlier anticipated, MASW and P-wave refraction measurements were performed. As for the refraction survey, the sources were placed at five locations along the receivers' line: at the WNW end, at 3 intermediate positions, and at the ESE end (Figure 3). At these shooting positions the sledgehammer was vertically blown on a flat metal plate. Two additional MASW shooting positions were placed WNN and ESE of the array, 12 m from the closest geophone (Figure 3); at these locations we used both a wedge-shaped plate for Love wave's excitation and flat plate for Rayleigh wave generation.

Figure 4: Geophone array in place with example of sledgehammer vertically blown. The picture was taken near the center of the line (view point ESE to WNW).

3.3 Acquisition

The time-sampling parameters adopted for both MASW and refraction acquisitions were the following: sampling interval = 125 μs, record length = 2 s, pre-trigger delay = -0.05 s.

At the seismic refraction source points, 10 hammer shots were blown; the traces generated by each blow were iteratively stacked and finally saved in a single .sg2 file.

As for the Rayleigh wave acquisition, at each of the two shot points 10 hammer blows were repeated; the traces generated by each shot were separately saved in an .sg2 file (without automatic stack).

For Love wave acquisition, at each shot point and at each of the two sides of the wedge plate 5 hammer shots were blown; the traces generated by each blow were iteratively stacked and finally saved in a single .sg2 file.

In Figure 5 we show sample seismic sections from P-wave refraction (left), Rayleigh wave (center) and Love wave (right) shots.

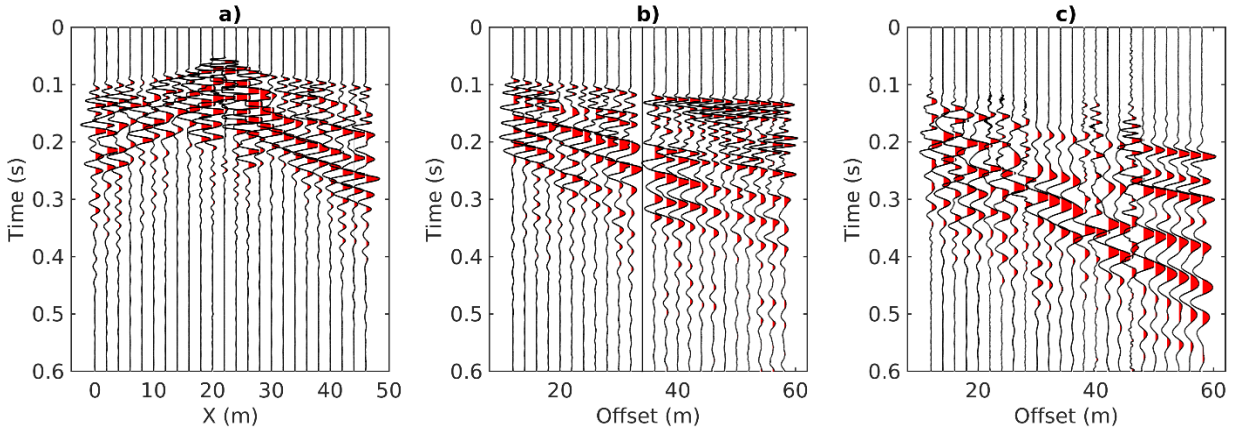

Figure 5: Examples of acquired seismic sections. a) Traces from a P-wave refraction shot (vertical component). The X coordinate is the distance from the easternmost geophone; b) traces from a Rayleigh wave shot (vertical component). The offset indicates the distance from the shooting position; c) traces from Love wave shots: the subplot displays the transverse-component traces obtained by subtracting the seismograms generated from the two opposite orientations of the source (i.e. hitting the two sides of the wedge-shaped plate). The offset indicates the distance from the shooting position.

3.4 Processing

3.4.1 Refraction processing

The P-wave first-break arrival times were manually picked on the stacked seismograms representing the vertical component of soil surface vibration. For completeness, P-wave arrivals were picked on the seismic sections from all available source positions (therefore including also Rayleigh-wave shots). Figure 6 represents the travel-time curves, or hodocrones, obtained from each source position.

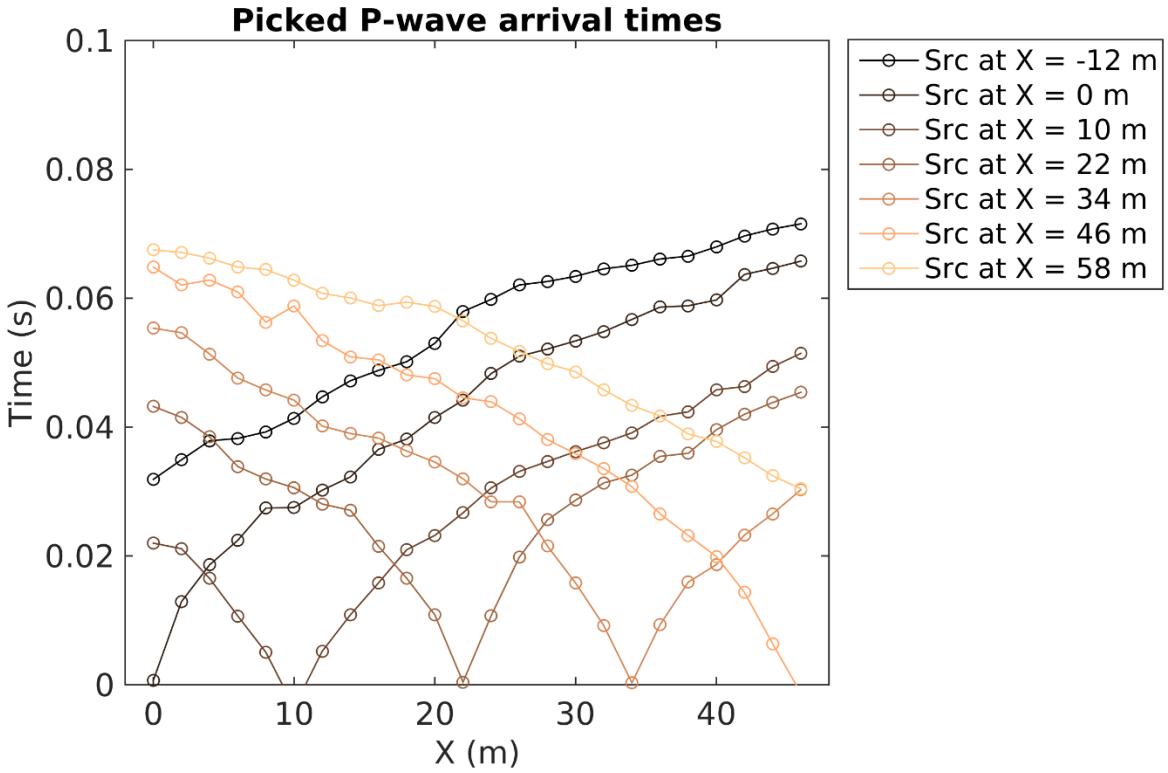

Figure 6 – P-wave refraction processing. Picked P-wave first-break arrival times from each shooting position. The X coordinate is the distance from the easternmost geophone.

3.4.2 Rayleigh wave data f-k processing

Rayleigh wave dispersion data were extracted from the vertical and radial component seismograms from MASW acquisitions. The considered seismic sections were processed by means of a 2D *f-k* (frequency – wavenumber) transform (Socco and Strobbia, 2004), in order to obtain a conversion of the recorded sets of traces from time–offset to frequency–wavenumber domain. *f-k* panels from single shot records with the same source position were summed to obtain spectral images with greater S/N ratio (O'Neill, 2003; Neducza, 2007). The energy maxima corresponding to the Rayleigh wave dispersion curves were picked on these stacked panels; spectral amplitude peaks from individual shot recordings were identified as well, and used to define the uncertainty intervals in the estimation of phase velocities (Socco et al., 2009; Boiero and Socco, 2010).

Figure 7 shows the stacked *f-k* panels from the considered seismic records, as well as the corresponding picked energy maxima. The dominant feature in all *f-k* spectra is a branch extending continuously in the 10-50 Hz frequency band, with wavenumbers between 0.1 and 1.5 rad/m. This feature is to be associated with the fundamental mode of Rayleigh wave propagation. At lower wavenumbers and higher frequencies other branches do exist and were picked. Their appearance is not necessarily coherent across all the four spectra, and they can be assigned to higher modes of Rayleigh wave propagation.

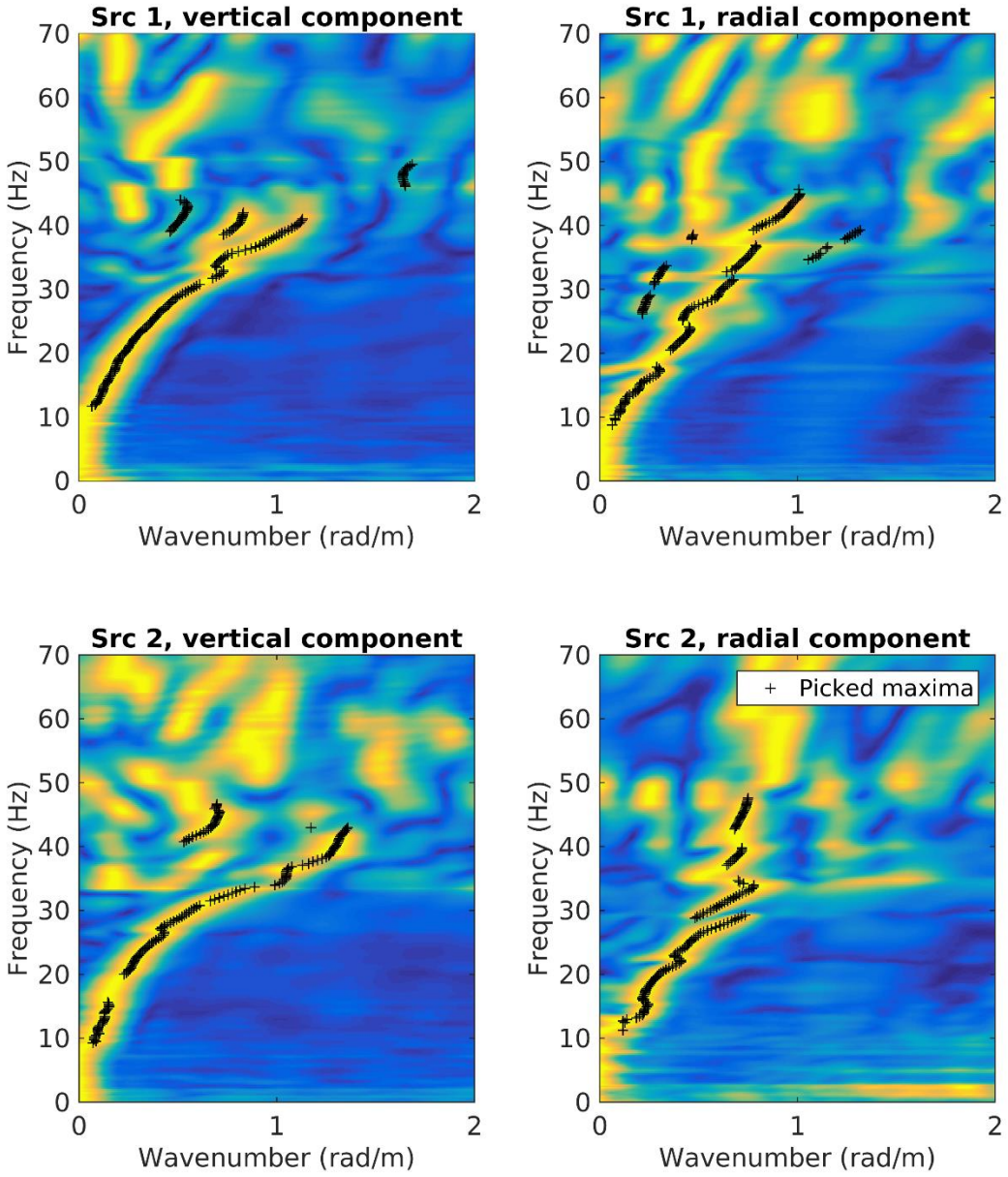

Figure 7: Stacked normalized f-k spectra obtained from vertical and radial components of the seismic section with source positioned 12 m from the easternmost geophone (Src 1), or 12 m from the westernmost receiver (Src2). Black crosses are the picked energy maxima, corresponding to Rayleigh wave dispersion curve data points.

For a careful modal attribution of the picked branches we followed an approach inspired by the procedures proposed by Maraschini and Foti (2010) and Abdel Moati et al. (2013) and extensively described in the site characterization report of station SBIK (Bergamo et al., 2018).
The basic idea is to test the agreement between the experimental apparent dispersion curve and a set of synthetic curves corresponding to a vast population of possible subsurface models, assuming a priori only the reliable modal attribution of few data points, and letting the others free to be assigned to the closest (in terms of phase velocity) simulated mode. The synthetic curve that best "explains" (i.e. closely matches) all (or most of) the experimental data points, and therefore achieves the lowest misfit, is assumed to propose the most likely modal attribution. The mode numbering resulting from this approach is shown in Figure 8.

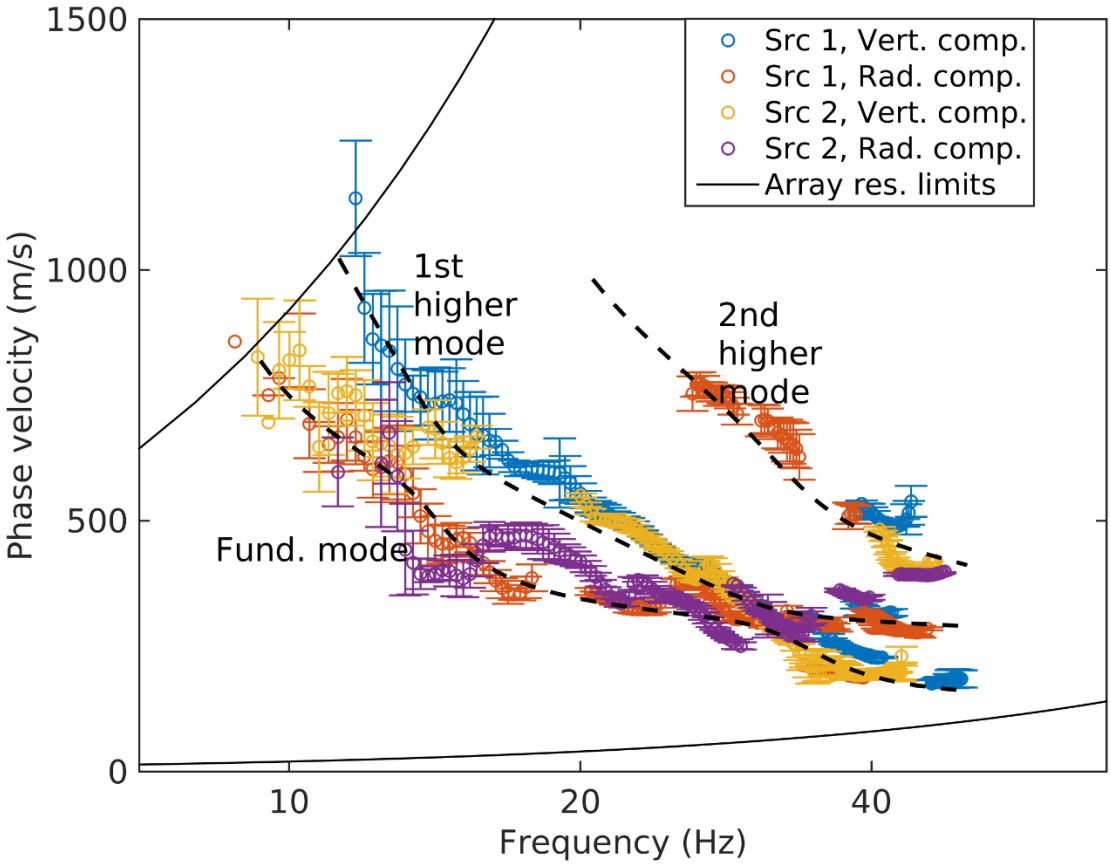

Figure 8: Multimodal Rayleigh wave dispersion curves obtained from f-k processing (picked on the four stacked f-k panels of Figure 7. The modal identification is represented with a dashed black curve.

The fundamental mode of Rayleigh waves extends continuously across all the available frequency band (8.8 – 45.5 Hz) with velocities decreasing from 800 to 200 m/s. Above the fundamental mode sparser dispersive branches were attributed to 1st and 2nd higher modes. Finally, the four curves obtained from each MASW source points (east and west of the array) and each component of propagation (vertical and radial) were merged into a single curve, representative for SENGL site.

3.4.3 Love wave data f-k processing

The hammer blows exerted on the slant faces of the wedge plate apply a two-component excitation to the ground: a vertical and a horizontal component, the direction of the latter depending on which face of the plate the stroke is given. Therefore, by summing the seismic traces obtained hitting the wedge on the two sides, the effects of the horizontal components are mutually eliminated, while the vertical components interact constructively; by computing the difference of the said seismograms, the vertical components nullify each other, while the horizontal components interact constructively (Schmelzbach et al., 2016; Sollberger et al., 2016). Consequently, the sum operator is equivalent to the use of a vertical blow; the difference operator is equivalent to a pure shear source (suitable for the observation of Love waves). As example, the panel to the right in Figure 5 represents the section obtained by computing the difference of the transversal component traces acquired when using the wedge-shaped plate (hence this common shot gather corresponds to a solely SH excitation).

Therefore, for the extraction of Love wave dispersion data, 2D f-k analysis was applied to the seismograms obtained as difference between the transversal components traces acquired when alternately hitting the two opposite faces of the wedge-shaped plate.

Figure 9 shows the f-k panel obtained from the shooting position easternmost for MASW (Love) analyses, as well as the picked energy maxima. The corresponding dispersion curve (Figure 10) comprises a fundamental mode extending from 7.8 to 53 Hz, with phase velocities decreasing from 700 to 200 m/s. The curve from shooting position 2 (west of the array) was not analyzed due to recording problems.

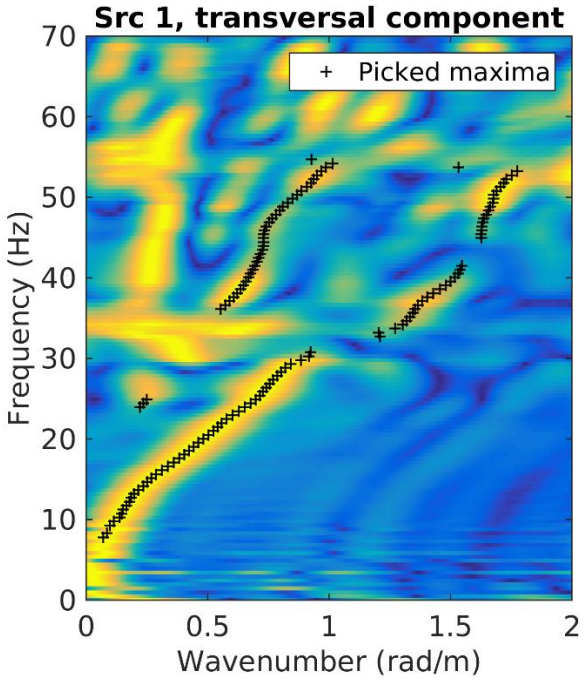

Figure 9: Normalized f-k spectra obtained from the difference of the seismic sections (transversal component) produced by alternately hitting the two sides of the wedge-shaped plate; src1 is the shooting point 12 m east of the array. Black crosses are the picked energy maxima, corresponding to Love wave dispersion curve data points.

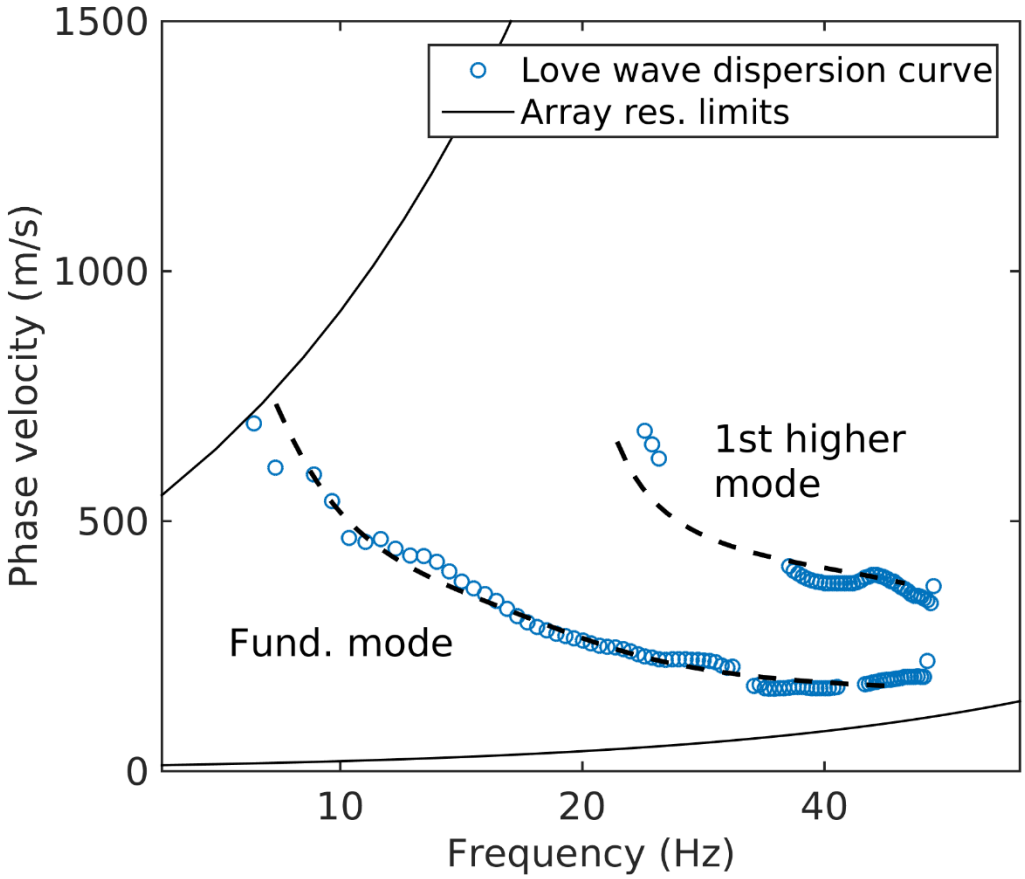

Figure 10 – Multimodal Love wave dispersion curves obtained from f-k processing (picked on the f-k panel of Figure 9). The modal identification is represented with dashed black lines.

3.4.4 WaveDecActive

To retrieve the properties of Rayleigh wave propagation in terms of phase velocity and ellipticity the seismic traces acquired for the Rayleigh wave survey were also processed with WaveDecActive code (Maranò et al., 2017). WaveDecActive implements a maximum likelihood algorithm for the analysis of Rayleigh waves generated by a controlled source. Key parameters required by WaveDecActive are the definition of the maximum number of Rayleigh waves that the code attempts to identify, and the value of parameter γ, which is able to modify the approach of the code towards wave identification from a Bayesian information criterion (γ=1) to a maximum likelihood approach (ML, γ=0) or a compromise between the two (0<γ<1). Following the recommendations of the code's author (Maranò, 2016) and some preliminary attempts, the maximum number of waves was set to 3 and γ to 0.2, thus opting for an approach close to a maximum likelihood solution. The obtained results are displayed in Figure 11, showing the estimated Rayleigh wave phase velocities (left panel) and ellipticity angles (right panel) for the considered shots.

Despite the fact that we filtered out, at each frequency, all the estimates with amplitude below the 10th percentile of the overall population, the results seem anyway quite confused, with many, segmented dispersive branches.
However, when superimposing the dispersion curve from f-k analysis (black line in Figure 11, left panel), it is possible to identify two branches following approximately the fundamental and first higher mode. We picked the (negative) ellipticity angle estimates along the Rayleigh wave fundamental mode to obtain the corresponding ellipticity curve (Figure 11, right panel). The obtained curve joins quite well at around 15 Hz with the ellipticity curve derived processing with RayDec (Hobiger et al., 2009) the single-station passive recordings.

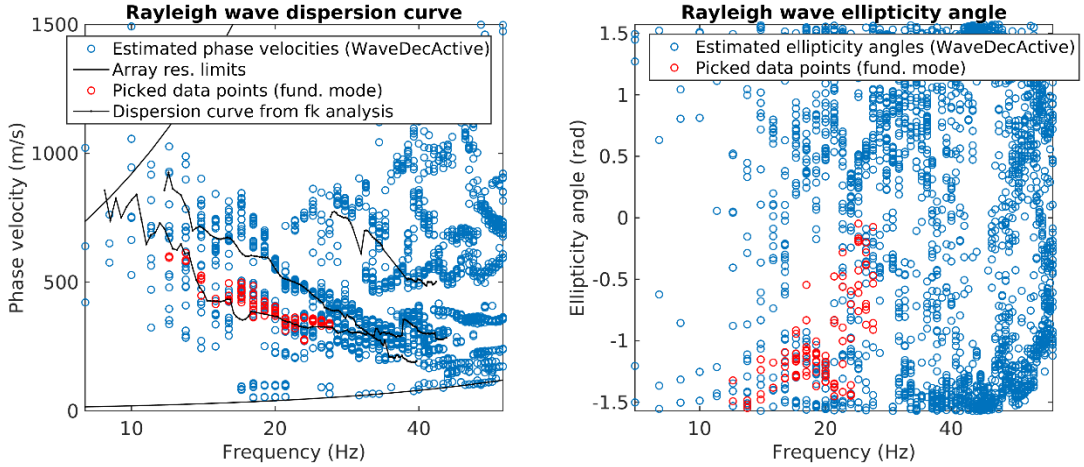

Figure 11 – Extraction of Rayleigh wave dispersion and ellipticity curve from WaveDecActive. Left: all estimated values of phase velocities (blue circles) and data points selected as belonging to the fundamental mode of Rayleigh wave propagation (red circles). Right: all estimated values of ellipticity angle (blue circles) and data points selected as belonging to the fundamental mode of Rayleigh wave propagation (red circles).

4 Passive seismic measurements

4.1 Acquisition and equipment

Beside the active seismic survey, single-station noise recording measurements were performed on the same acquisition day. One measurement was performed just few meters from SENGL, whereas a second one was made near the active seismic line (Figure 3). In both cases, the sensor (Lennartz 3C 5s seismometer) was placed on a metal tripod in contact with the ground (Figure 12). The sampling frequency was 200 Hz and the recording spanned a 40-minute time interval; a Centaur datalogger was employed.

Figure 12 – Single-station ambient vibration recording performed nearby the SENGL seismic station.

4.2 Processing

The passive traces were processed with the aim of:

- estimating the H/V ratio of recorded noise, thus identifying the fundamental frequency of resonance of the site (Nakamura, 1989) by the use of classical H/V methods (as implemented in Geopsy software, www. geopsy.org; classical H/V of Fäh et al., 2001).
- estimating the ellipticity of Rayleigh wave as a function of frequency by resorting to refined algorithms (Raydec, Hobiger at al., 2009; time-frequency method, Poggi and Fäh, 2010; wavelet-based time-frequency method as implemented in Geopsy software).

To obtain a more reliable estimation of Rayleigh wave ellipticity the latter methods aim at eliminating the contributions of other waves besides Rayleigh waves, when compared to the classical H/V technique.

The results are shown in Figure 13. All applied techniques yield similar H/V or ellipticity curves, except TFA1 and TFA3 on which is possible to observe a peak at around 1.5 Hz. Moreover, the general HVSR amplitude at the station ENGL01 (close to SENGL) tends to increase its amplitude gradually at higher frequency, showing a broadband distribution of peaks, which can usually be associated to alternating layers with different velocities.

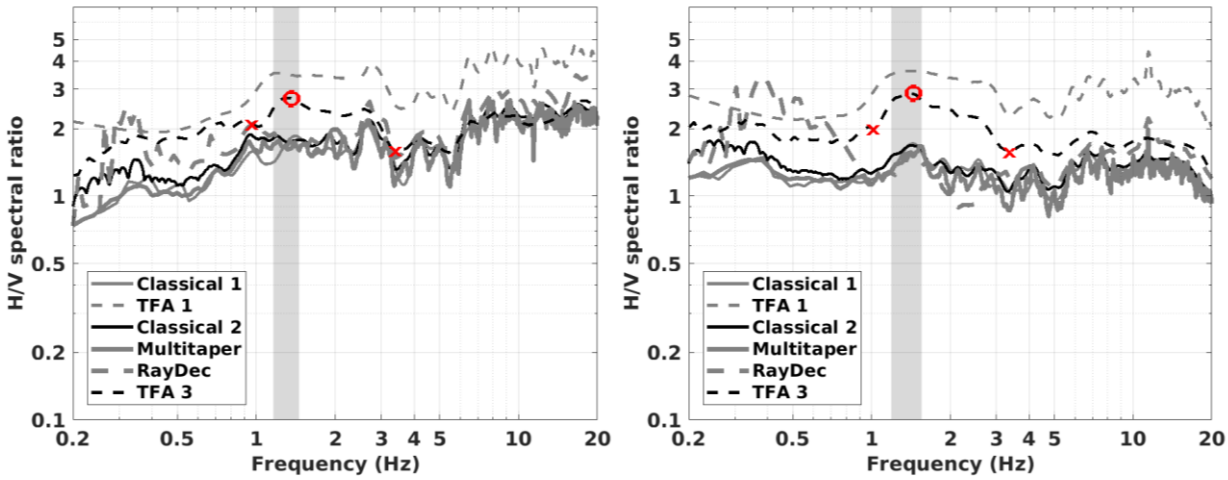

Figure 13 – H/V ratio and ellipticity curves obtained from the processing of noise recording data, using several algorithms at the sites ENGL01 (left panel) and ENGL02 (right panel). Classical 1: Geopsy; Classical 2: Fäh et al., 2001; TFA1: wavelet-based time-frequency method as implemented in Geopsy software; TFA3: time-frequency method, Poggi and Fäh, 2010; Raydec: Hobiger et al., 2009. Picked resonance frequencies are indicated by red circles; the corresponding intervals are marked by red crosses.

The recordings from the passive sensors were also processed with the polarization tool of Burjanek et al. (2010). In Figure 14 we display the produced ellipticity (as defined in Burjanek et al., 2010) and strike/dip graphs as a function of frequency. The ellipticity plots (Figure 14, right) show a clear trough at ~1.5 Hz, which corresponds to the H/V peaks in Figure 13. For the polar strike (Figure 14, left), a moderate directionality effect can be identified for the 1.5 Hz peak along the WSW-ENE direction. This direction corresponds to the maximum slope direction, which could produce this effect.

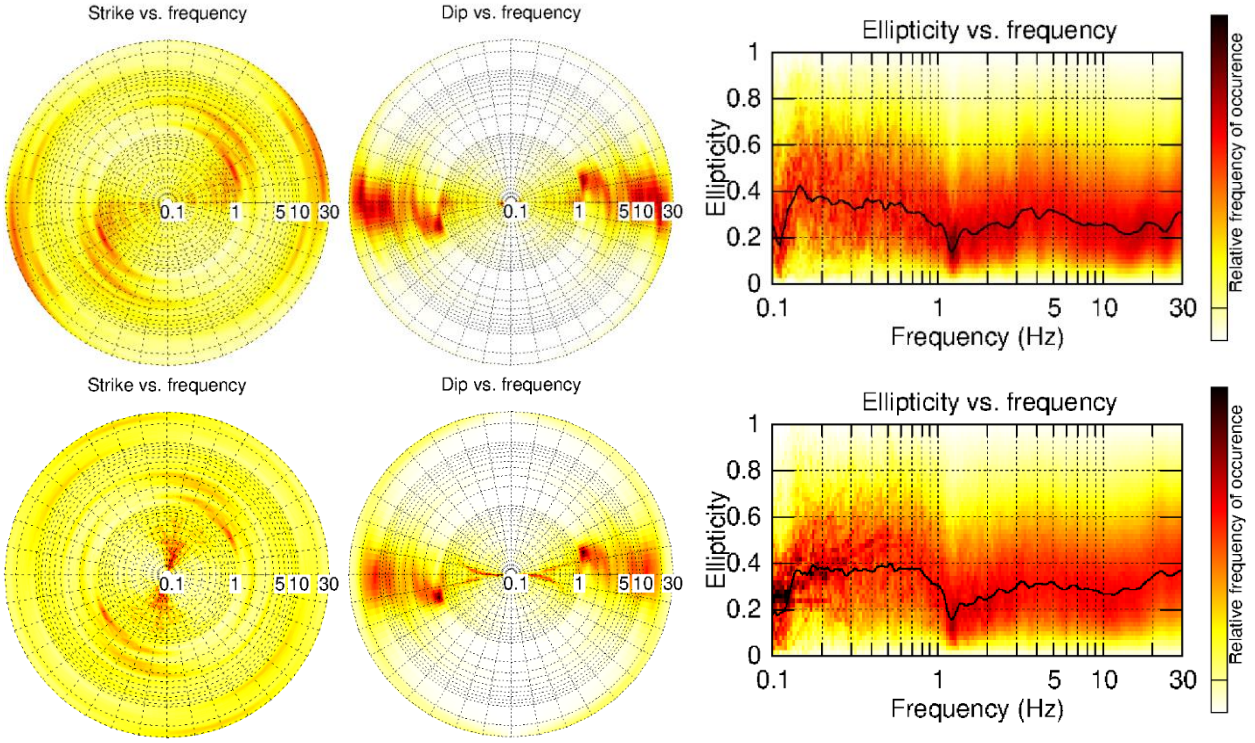

Figure 14 – Polarization analysis at the seismic station ENGL01 (upper panels) and ENGL02 (lower panels). From left to right, strike vs. frequency, dip vs frequency and ellipticity vs frequency graphs. Description on the computation method can be found in Burjanek et al. (2010).

5 P-wave velocity profile

P-wave first-break arrival times were manually picked on the vertical-component seismograms. The complete set of obtained travel-time curves (one from each considered shooting position) is shown in Figure 6. The hodocrones appear to be approximately symmetrical, i.e. the P-wave travel time depends only on the source-to-receiver distance and not on the position of the shot point. This suggests a 1D geometry (no or little lateral variations) for the near-surface below the active seismic arrays.

Collected refraction data were interpreted with the method of intercept time analysis (Reynolds, 2011). Following the hypothesis of a 1D geometry for the shallow subsurface (see above), the hodocrones obtained from refraction processing were collapsed into a single travel-time curve in time-offset domain (Figure 15). The resulting surficial velocity profile is shown in Figure 15. A 3-layer over halfspace model was obtained, with V_P increasing from 202 m/s (surface) to around 1900 m/s (14 m depth).

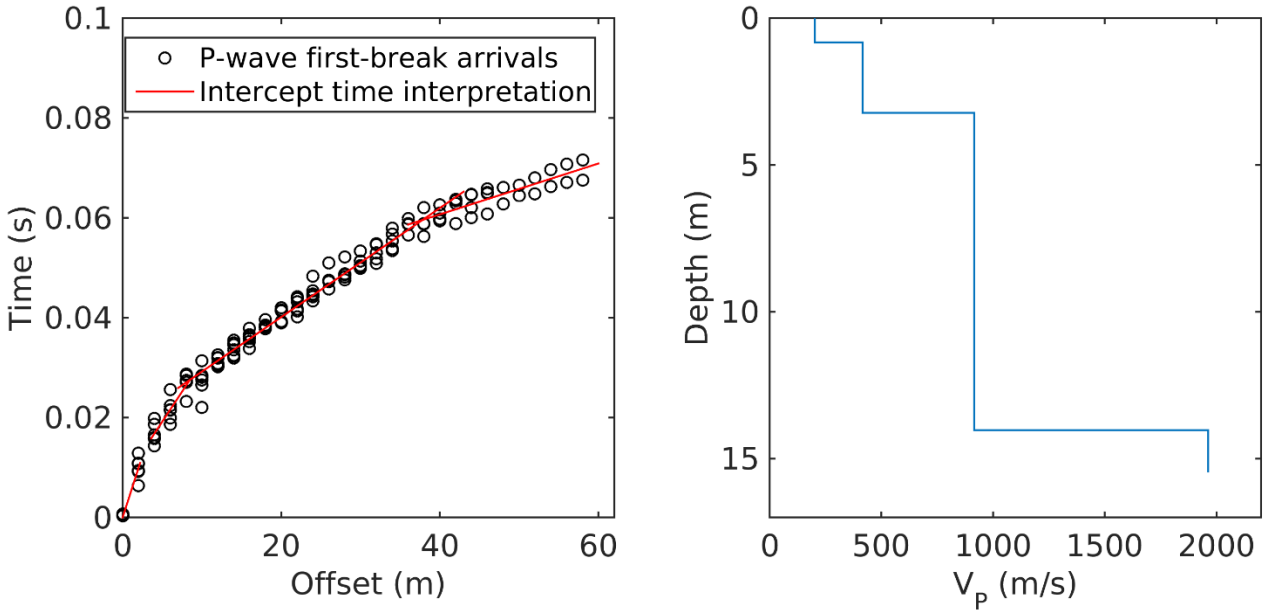

Figure 15 – Left pane: plot of travel-time-vs-distance for the seven shots (black dots). The red lines are the limit imposed for the construction of 1D initial velocity models. Red broken line (4 segments) shows the 1D model selected for the inversion. Right panel: obtained 1D velocity model for V_P.

6 Inversion of surface wave data

The Love and Rayleigh wave dispersion and ellipticity curves obtained from the processing of active and passive seismic data were inverted for the 1D S-wave velocity profile of the investigated site. For the inversion the dinver code implemented in Geopsy was used. The code provides a set of Vp/Vs models compatible with the observed dispersion curve. This inversion tool uses a directed-search method, called "neighbourhood algorithm" (Sambridge, 1999).

6.1 Inversion target

The target we selected for the inversion (Figure 16) consists of:

- The multimodal Rayleigh wave dispersion curve, as obtained from the processing of active data with the f-k processing.
- The multimodal Love wave dispersion curve, as obtained from the processing of active data with the f-k processing.
- The Rayleigh wave ellipticity curve for the fundamental mode from ENGL02 single-station passive recording processed with Raydec between 2.0 and 28.0 Hz was considered.

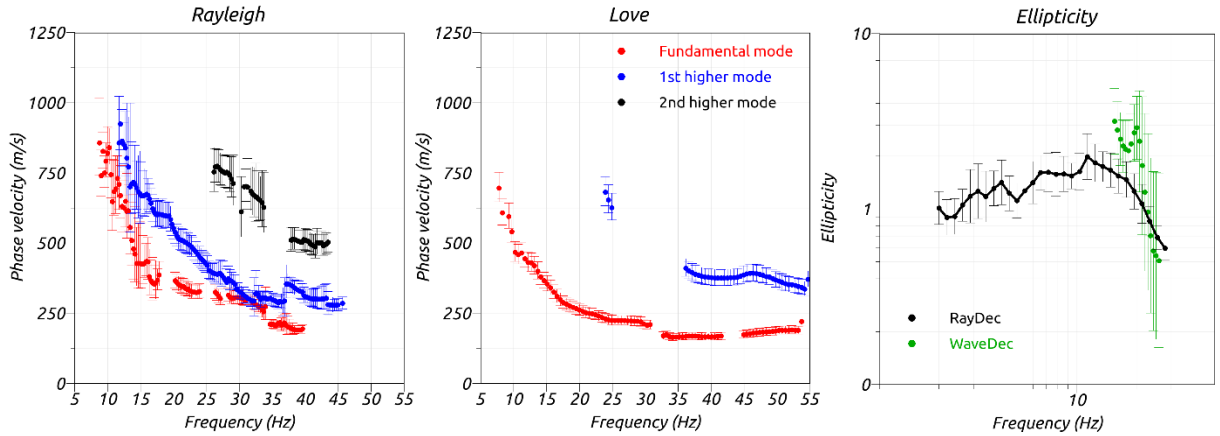

Figure 16 – Target of surface wave dispersion and ellipticity curves for the inversion process. Left: multimodal Rayleigh wave dispersion curve obtained from the processing of active data with f-k processing. Center: multimodal Love wave dispersion curve obtained from the processing of active data with f-k processing. Right: ellipticity curve for the fundamental mode of Rayleigh wave; the low-frequency portion was obtained by processing passive data (ENGL02) with Raydec code; the high-frequency portion was obtained from the processing of active data with Wavedec code.

6.2 Parameterization of the model space

For the parameterization of the subsurface model two different strategies were followed: the soil column was modelled as a stack of 3 to 7 homogeneous layers with variable thickness overlying an halfspace. In both parameterizations at each layer the V_S can vary within broad boundaries (100-1500 m/s). The same applies to V_P (200-5000), although the resulting V_S/V_P ratio must be compatible with a range of possible values of Poisson's ratios set for each layer: 0.2 – 0.4. The density values are attributed to each layer as equal to 1.9 t/m^3 and 2.3 t/m^3 for the halfspace. For each parameterization we completed an inversion run with 2x10^5 models.

6.3 Inversion results

We performed a total of 6 inversions with different number of layers (see Table 1) using the Dinver routine (http://www.geopsy.org/). Each inversion run produced 200000 total models in order to assure a good convergence of the solution. The results of these inversions are shown in Figs 17 – 24

Table 1: List of inversions

Inversion	Number of layers	Number of models	Minimum misfit
SENGL 4l	4	200000	0.74303
SENGL 5l	5	200000	0.75076
SENGL 6l	6	200000	0.77871
SENGL 7l	7	200000	0.81918
SENGL 8l	8	200000	0.83677
SENGL fix	19	200000	0.84759

The 4-layer parametrization yields slightly lower misfit values (Tab. 1), however the velocity profiles are generally consistent. The data fit is reasonably good for both surface wave dispersion and ellipticity curves.

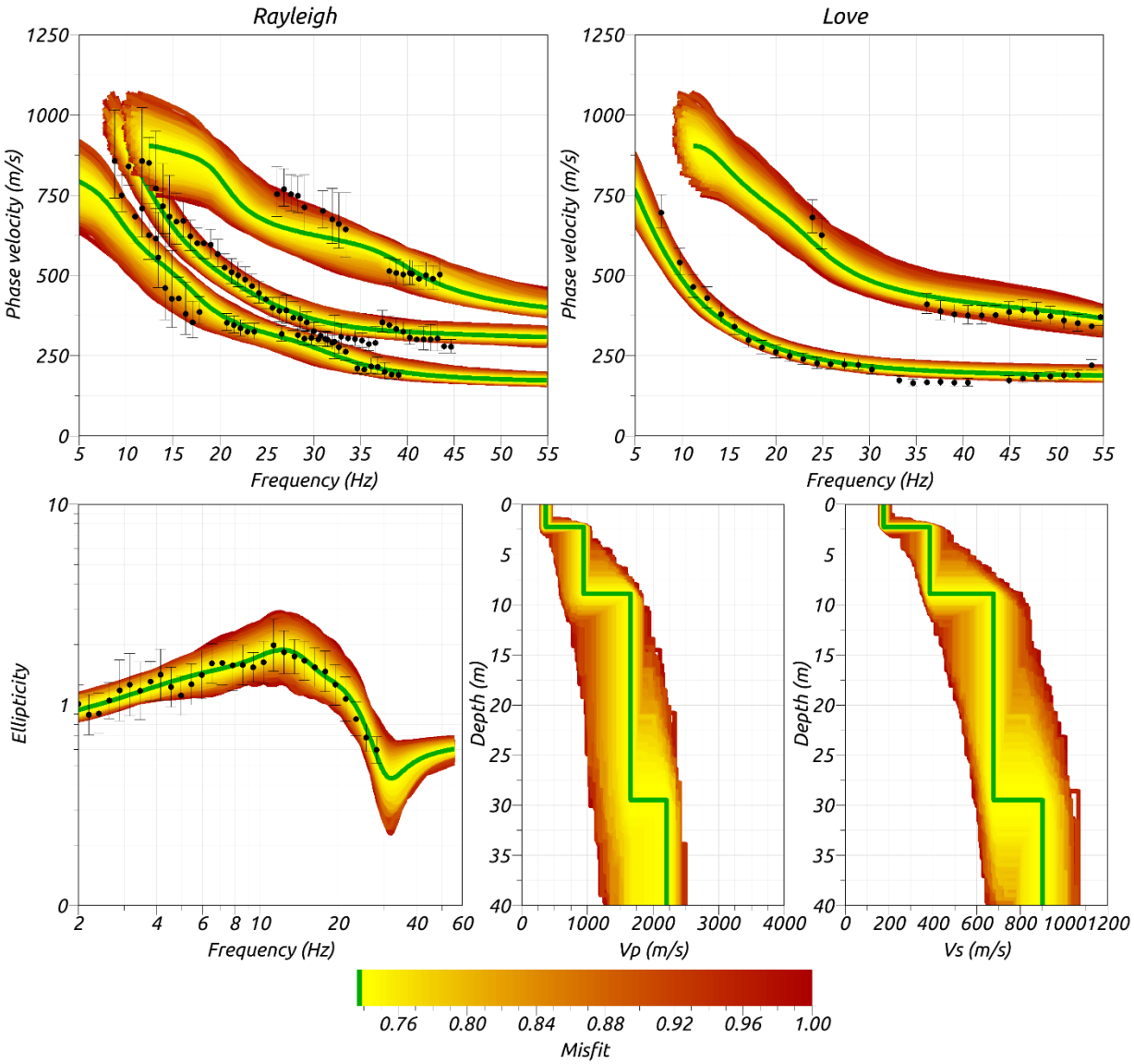

Figure 17: Inversion SENGL4l. Top line: Dispersion curves for the Rayleigh and Love waves. Bottom line: Ellipticity curve (left), P-wave velocity profiles (center) and S-wave velocity profiles (right). The black dots indicate the data points used for the inversion. The green line indicates the best-fitting model.

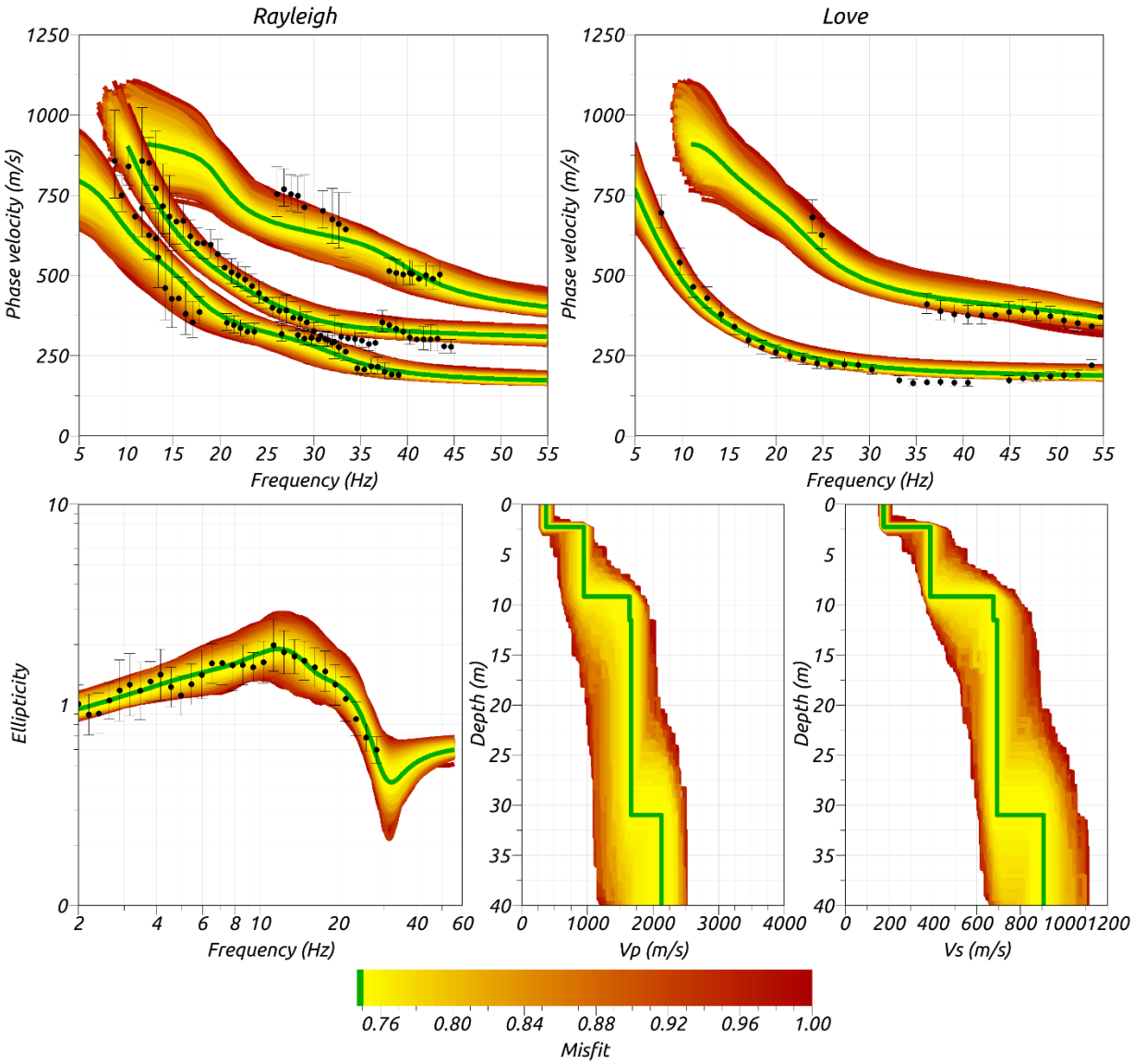

Figure 18: Inversion SENGL5l. Top line: Dispersion curves for the Rayleigh and Love waves. Bottom line: Ellipticity curve (left), P-wave velocity profiles (center) and S-wave velocity profiles (right). The black dots indicate the data points used for the inversion. The green line indicates the best-fitting model.

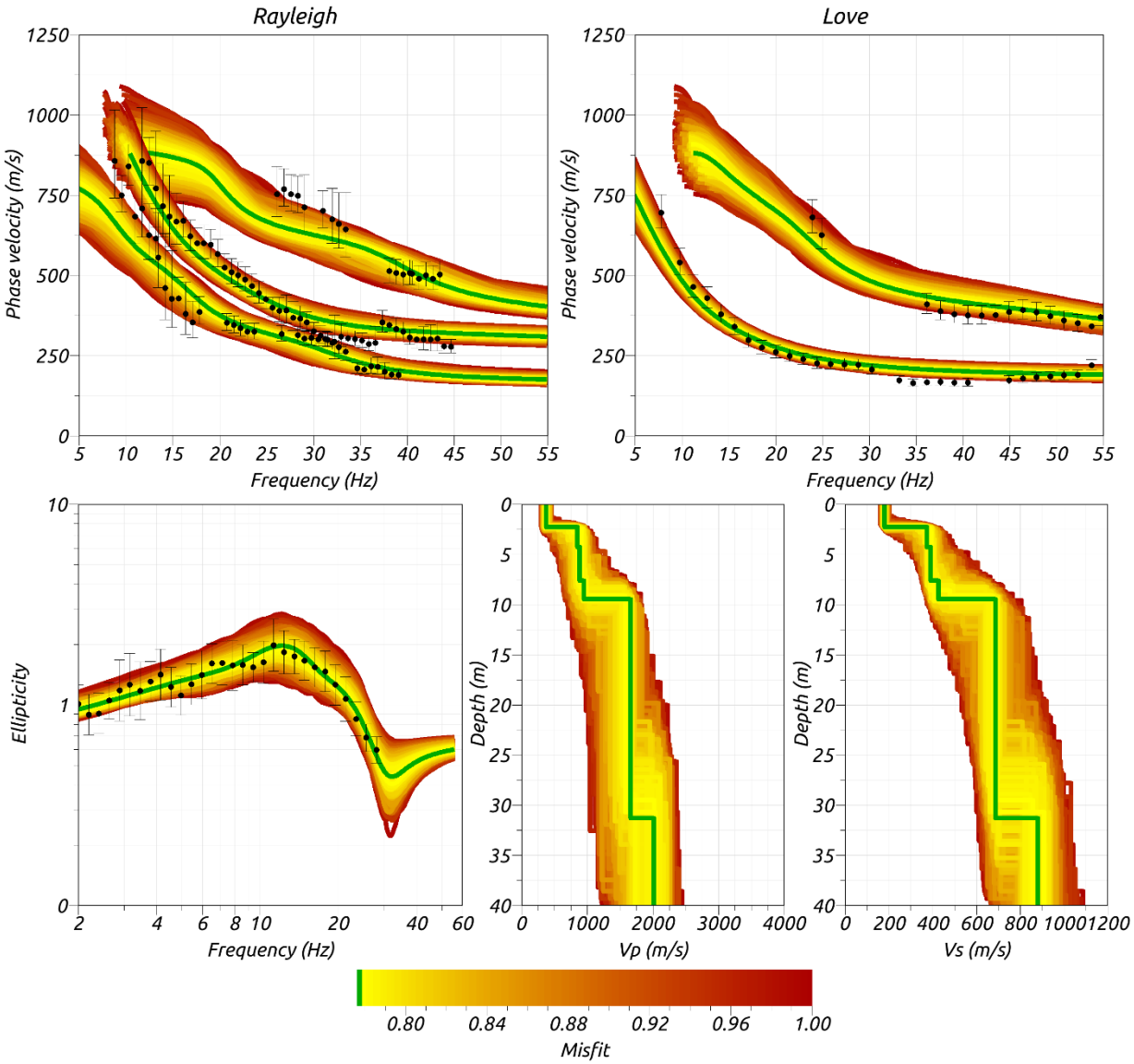

Figure 19: Inversion SENGL6l. Top line: Dispersion curves for the Rayleigh and Love waves. Bottom line: Ellipticity curve (left), P-wave velocity profiles (center) and S-wave velocity profiles (right). The black dots indicate the data points used for the inversion. The green line indicates the best-fitting model.

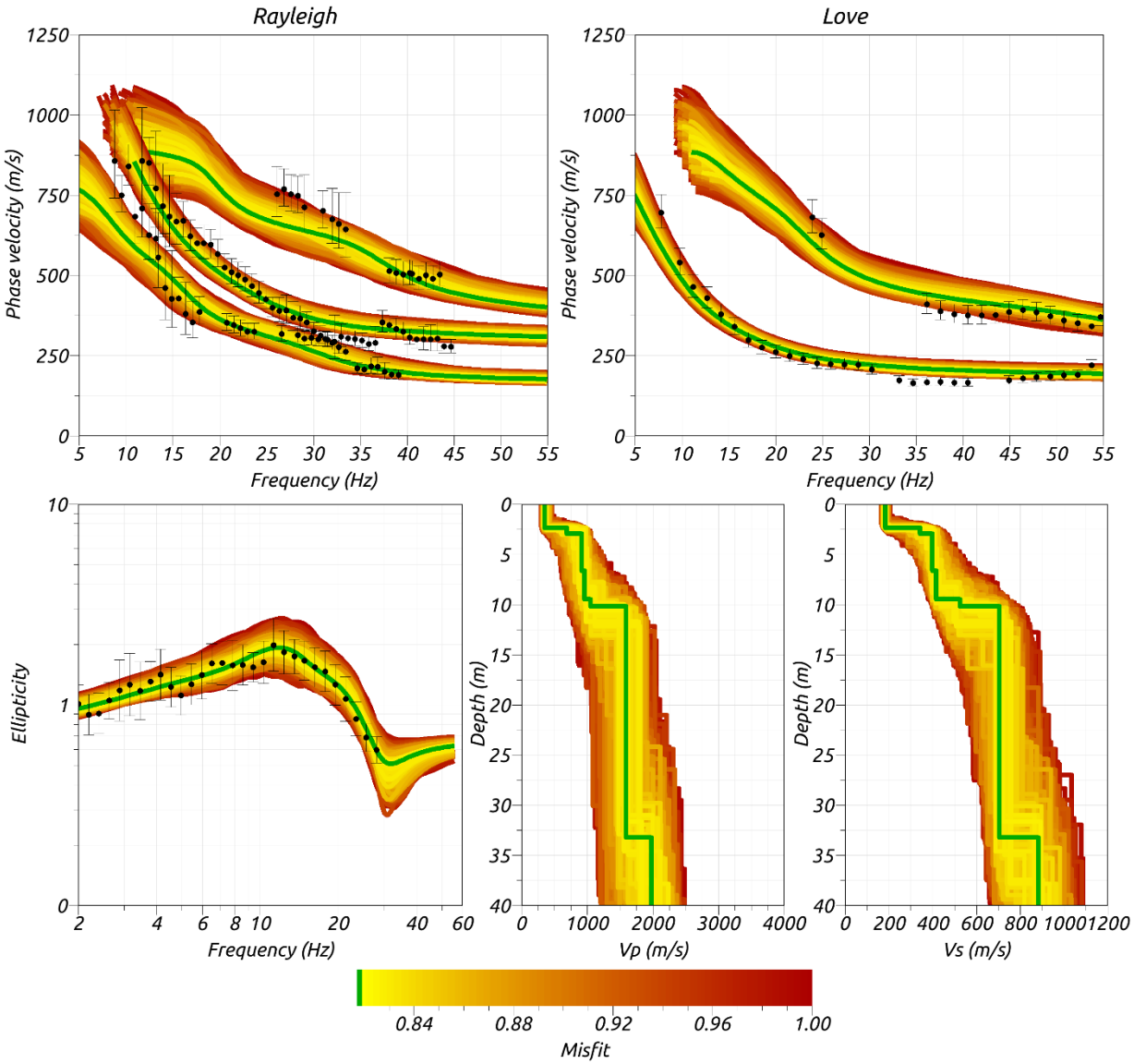

Figure 20: Inversion SENGL7l. Top line: Dispersion curves for the Rayleigh and Love waves. Bottom line: Ellipticity curve (left), P-wave velocity profiles (center) and S-wave velocity profiles (right). The black dots indicate the data points used for the inversion. The green line indicates the best-fitting model.

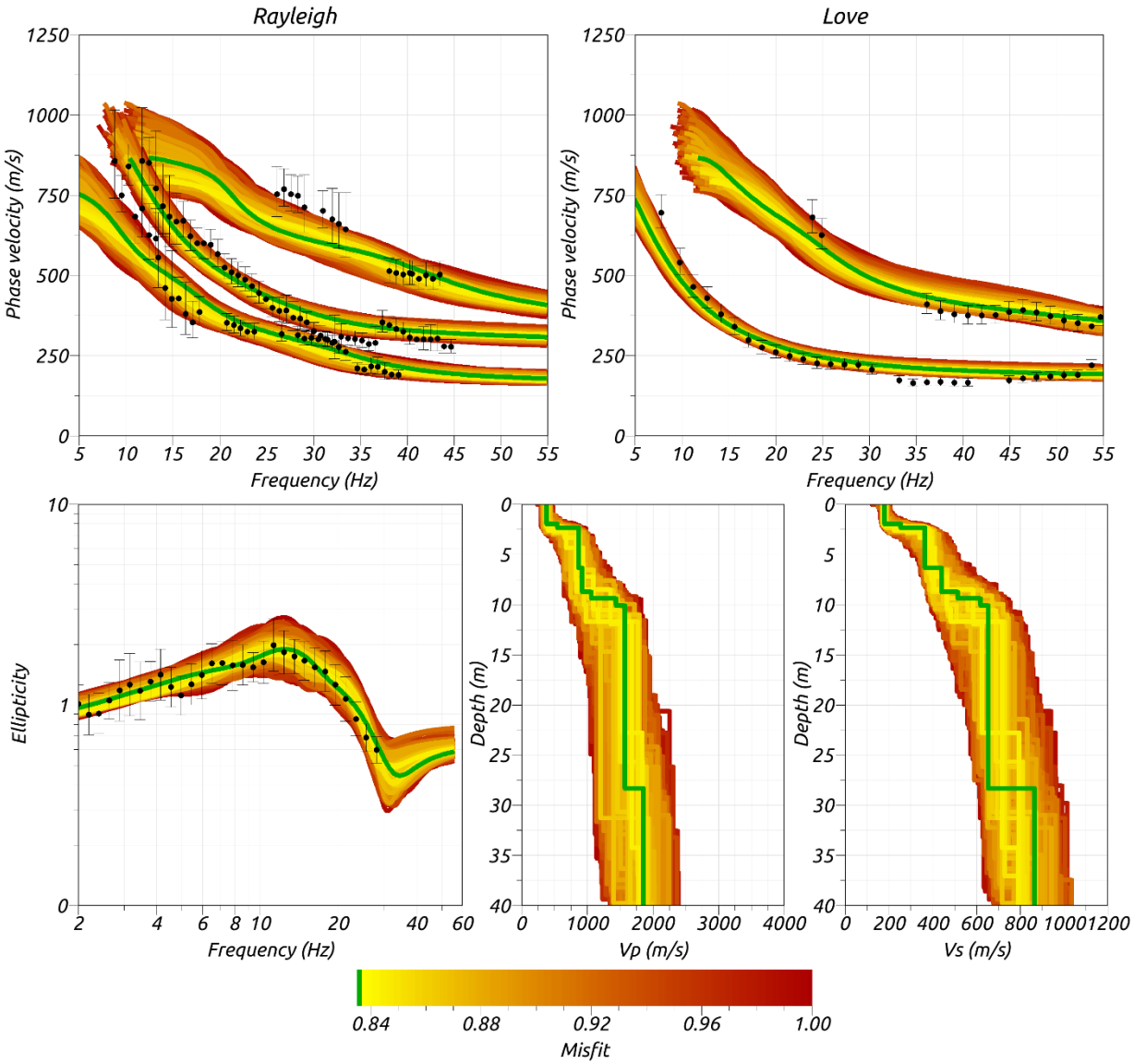

Figure 21: Inversion SENGL8l. Top line: Dispersion curves for the Rayleigh and Love waves. Bottom line: Ellipticity curve (left), P-wave velocity profiles (center) and S-wave velocity profiles (right). The black dots indicate the data points used for the inversion. The green line indicates the best-fitting model.

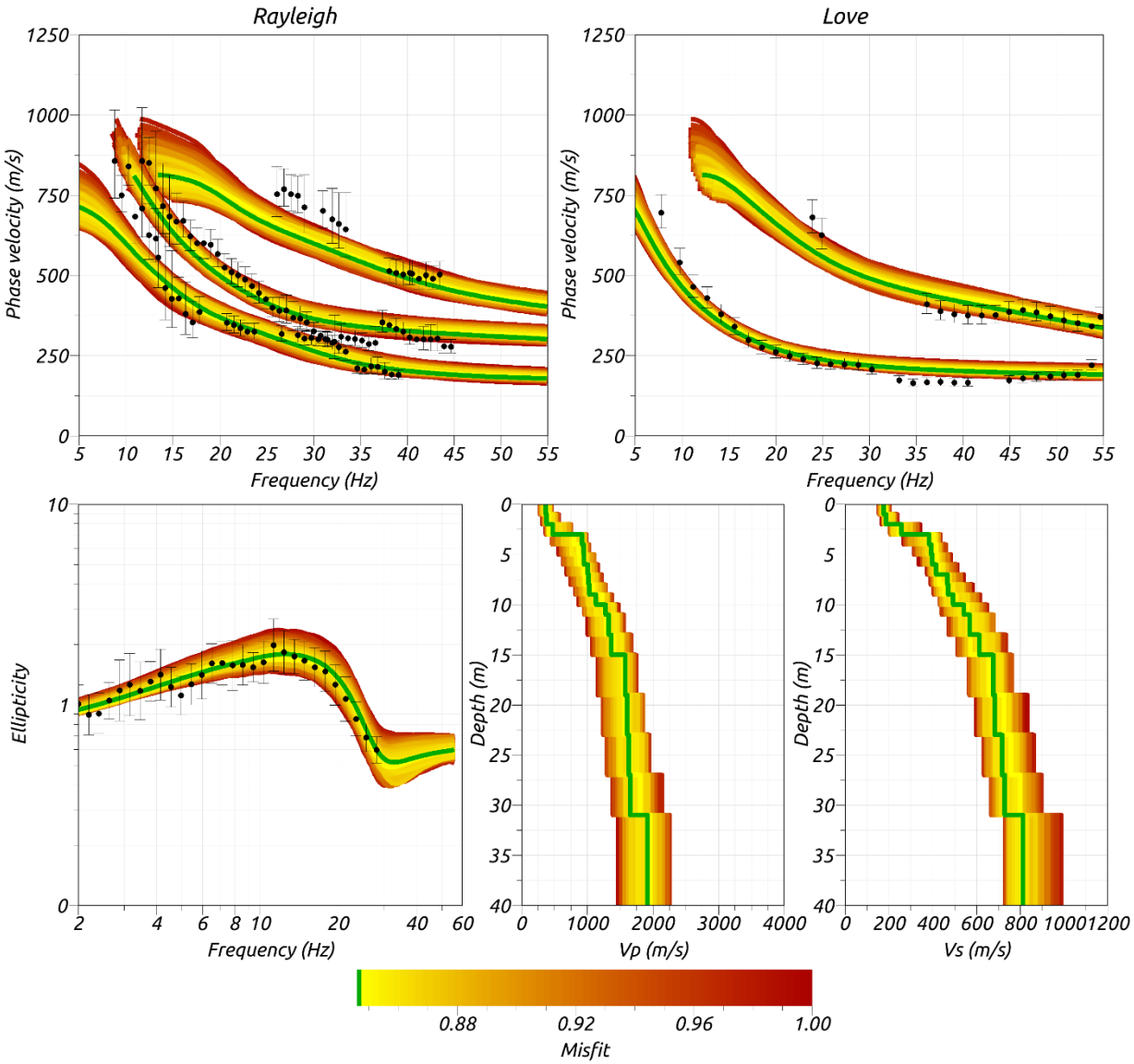

Figure 22: Inversion SENGLfix. Top line: Dispersion curves for the Rayleigh and Love waves. Bottom line: Ellipticity curve (left), P-wave velocity profiles (center) and S-wave velocity profiles (right). The black dots indicate the data points used for the inversion. The green line indicates the best-fitting model.

7 Interpretation of the velocity profiles

7.1 Velocity profiles

The 6 best performing (i.e. lowest misfit) models from chosen layer parametrization inversions are considered as final result (Figure 23).

The upper 2-3 m have a V_S around 190 m/s, and they are presumably composed of weathering soil. Below, we meet two layers, with thicknesses of around 7 and 20 m, and S-wave velocity increasing from 380 to 680 m/s; these layers should correspond to the conoid formation indicated by the geological map (Figure 2). In the same depth range (0 – 10 m), we notice that the estimated V_P from surface wave data inversion agree with the velocities obtained from refraction tomography (red line in Figure 23). The only discrepancy between V_P and V_S profiles is observed for the second discontinuity, that seismic refraction locates 4 m down (about 14 m depth) with respect the best profiles obtained with dispersion curves inversion (about 10 m depth). At a depth of ~30 m, S-wave velocity increases to about 900 m/s, but the velocity contrast is not sharp, indicating a gradually increase with depth.

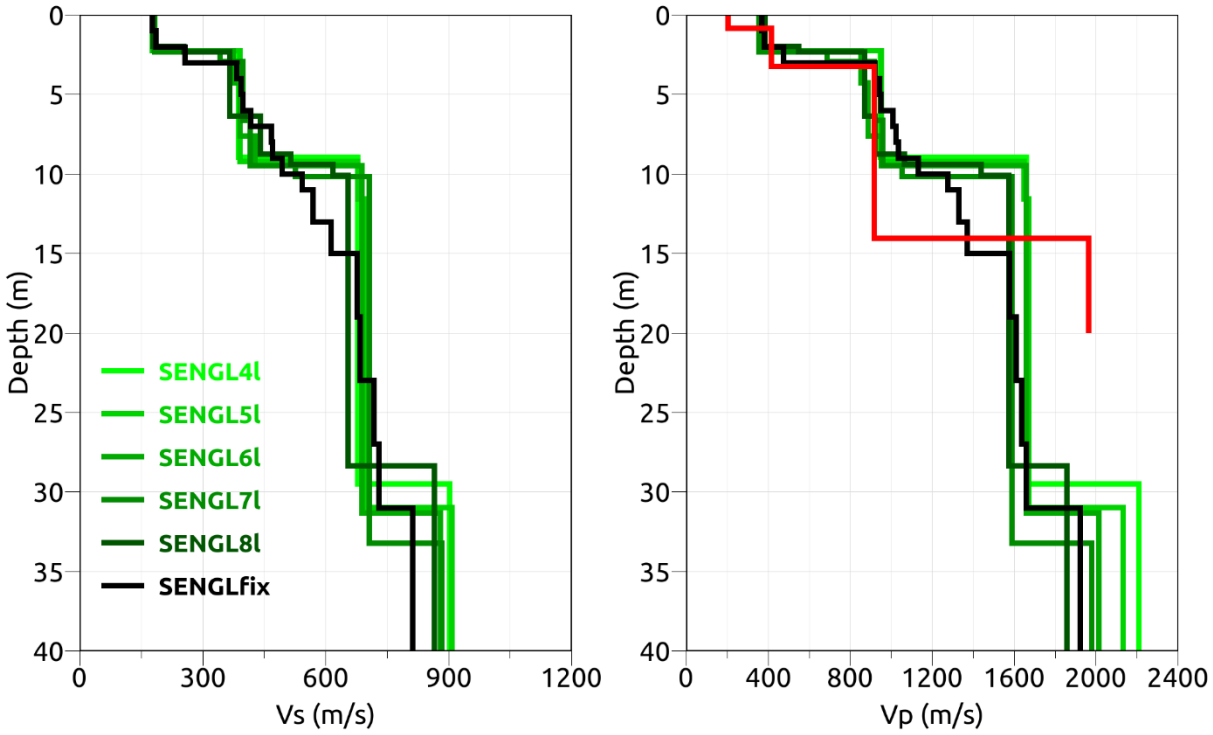

Figure 23: Overview of the best shear-wave velocity profiles of the different inversions for V_S (left) and V_P (right). The red line in the right panel is the V_P profile obtained through seismic refraction.

7.2 Quarter-wavelength representation

The quarter-wavelength velocity approach (Joyner et al., 1981) provides, for a given frequency, the average velocity at a depth corresponding to 1/4 of the wavelength of interest. The results using this proxy, considering frequency limits of the experimental data is well constrained above 30 m (Fig. 24). The quarter wavelength impedance-contrast introduced by Poggi et al. (2012) is also displayed in the figure. It corresponds to the ratio between two quarter-wavelength average velocities, respectively from the top and the bottom part of the velocity profile, at a given frequency.

The SENGL station is located at an altitude of 1033 m a.s.l., which is 2-3 m higher than the active seismic line location. We took this into account, to adjust the obtained velocity profiles to the station location. In particular, the thickness of the first layer, linked to the weathering soil, was increased of 2 m and the quarter-wavelength velocity approach was re-applied to the new adjusted profiles (Fig. 24 right panels).

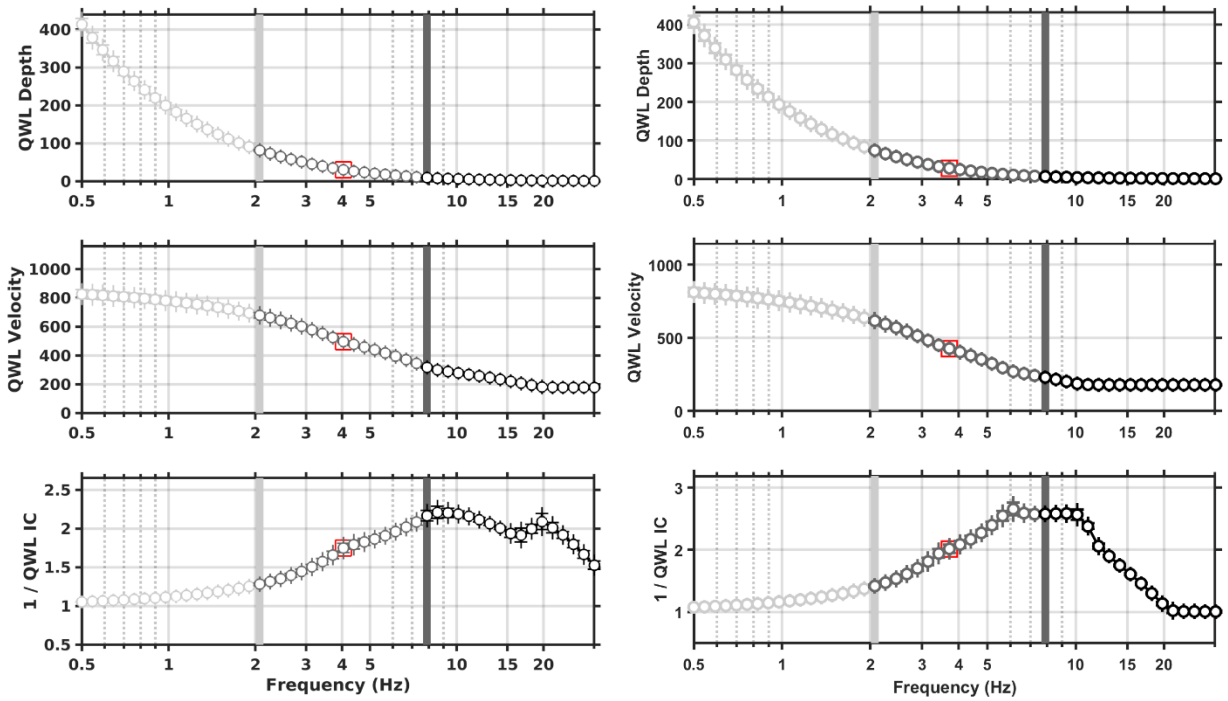

Figure 24: Left panels: quarter wavelength representation of the velocity profiles for the best models of the inversions (top: depth, center: velocity, bottom: inverse of the impedance contrast). Right panels: quarter wavelength representation of the adjusted velocity profiles to the station location. The grey light bar shows the ellipticity lower frequency value, dark grey bar indicates the lower frequency value obtained with dispersion curves and red square corresponds to f_{30} (frequency related to the depth of 30 m).

7.4 Amplification function

In Figure 25, the average theoretical SH-amplification relative to the Swiss reference rock profile from the obtained models and adjusted ones are shown (black lines). The adjustment of the first layer thickness improves the match for the seismic station location. In this case, the models are predicting an amplification up to a factor of 4.0 at frequency higher than 9.0 Hz, which is in quite good agreement with the peak observed in the empirical amplification function. The present (24.02.2020) amplification from empirical spectral modeling (red line) is not stable considering the low number of earthquake used for its computation; the main disagreement between observed and predicted amplification is the amplitude. As soon as the station has recorded a sufficient number of earthquakes the comparison will be repeated.

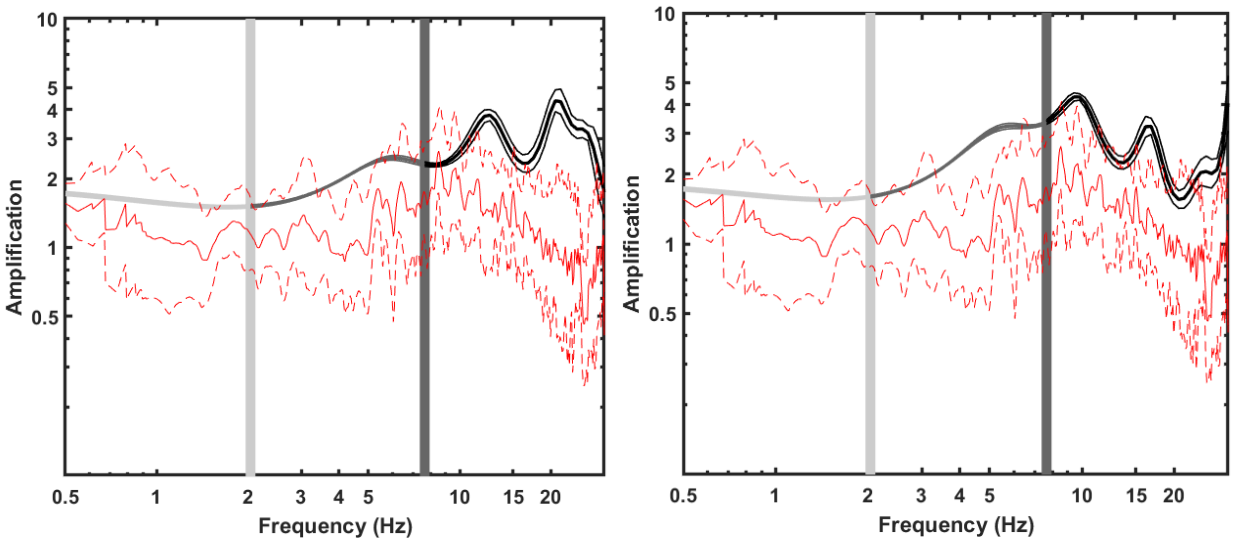

Figure 25: Modeled amplification function for the best velocity models of the six inversions (left panel). Modeled amplification function for the adjusted velocity models of the six inversions to take into account the station quote (right panel). Red continuous line is the average empirical amplification function at the SENGL station, whereas dashed red lines are the standard deviations.

6 Discussion and conclusions

The general HVSR amplitude at the station ENGL01 (close to SENGL) tends to increase its amplitude gradually at higher frequency, showing a broadband distribution of peaks, which can usually be associated to alternating layers with different velocities. Moreover, a quite evident peak is observed at around 1.5 Hz, possibly related to a rock/rock deep interface not resolved by our measurements or to a slope effect, as highlighted by polarization results.
The inversion of the active seismic measurements yields a velocity profile with 3 main interfaces at about 2 m, 10 m and 30 m depth. In particular, the soft layer has a velocity increasing with depth from 190 to 680 m/s reaching a velocity of about 900 m/s at 30 m depth. The V_{S30} value of the site is determined as about 493 m/s, corresponding to soil class B in EC8 (CEN, 2004) and C in SIA261 (SIA, 2014) classifications. The theoretical SH-amplification relative to the Swiss reference rock profile predicts an amplification factor 4 at a frequency of 9.0 Hz, in quite good agreement with the amplification observations at this station.

Acknowledgements

The authors thank Paulina Janusz for her help during the measurements.

References

Abdel Moati W.H., D. Boiero, and L.V. Socco, 2013. A tool for fast underground characterization for trenchless pipeline construction by horizontal directional drilling technology. 11th Offshore Mediterranean Conference and Exhibition, Ravenna, Italy, March 20-22 2013.

Bergamo P., M. Hobiger and D. Fäh, 2018. Site characterization report, SBIK – Biel/Bienne (BE), Kongresshaus/Palais des Congrès. Swiss seismological service (SED)

Boiero, D., and L. V. Socco, 2010. Retrieving lateral variations from surface wave dispersion curves analysis: Geophysical Prospecting, 58, 977–996

Burjanek J., G. Gassner-Stamm, V. Poggi, J.R. Moore and D. Fäh, 2010. Ambient vibration analysis of an unstable mountain slope, GJI, 180, 820-828.

CEN, 2004. Eurocode 8: Design of structures for earthquake resistance – Part 1: general rules, seismic actions and rules for buildings. European Committee for Standardization, en 1998-1 edition.

Edwards, B., Michel, C., Poggi, V., and Fäh, D., 2013. Determination of Site Amplification from Regional Seismicity: Application to the Swiss National Seismic Networks. Seismological Research Letters, 84(4).

Fäh, D., F. Kind, and D. Giardini, 2001. A theoretical investigation of average H/V ratios. GJI, 145, no. 2, 535-549.

Herrmann, R. B., 2013. Computer programs in seismology: An evolving tool for instruction and research, Seism. Res. Lettr. 84, 1081-1088, doi:10.1785/0220110096

Hobiger, M., P.-Y. Bard, C. Cornou, and N. Le Bihan, 2009. Single station determination of Rayleigh wave ellipticity by using the random decrement technique (Raydec). GRL, 36, L14303

Joyner, W. B., Warrick, R. E., and Fumal, T. E., 1981. The effect of Quaternary alluvium on strong ground motion in the Coyote Lake, California, earthquake of 1979. Bulletin of the Seismological Society of America, 71(4):1333–1349.

Lanz E., H. Maurer and A. G. Green, 1998. Refraction tomography over a buried waste disposal site. Geophysics, 63 (4), 1414-1433.

Marano' S., 2016. http://mercalli.ethz.ch/~marra/WaveDec/userguide_WaveDec.html

Marano, S., Hobiger M., P. Bergamo and D. Fäh, 2017. Analysis of Rayleigh Waves with Circular Wavefront: a Maximum Likelihood Approach. GJI, 210, 1570-1580.

Maraschini M., and S. Foti, 2010. A Monte Carlo multimodal inversion of surface waves. GJI, 182 (3). 1557 – 1566.

Nakamura, Y., 1989. A Method for Dynamic Characteristics Estimation of Subsurface Using Microtremor on the Ground Surface. Quarterly Report of RTRI, vol. 30, no. 1, 25- 33.

Neducza, B., 2007, Stacking of surface waves: Geophysics, 72, 51–58.

O'Neill, A., 2003, Full-waveform reflectivity for modelling, inversion and appraisal of seismic surface wave dispersion in shallow site investigations: PhD thesis, University of Western Australia, Perth, Australia.

Park, C. B., R. D. Miller, and J. Xia, 1999. Multichannel analysis of surface waves: Geophysics, 64, 800–808.

Poggi, V., B. Edwards and D. Fäh, 2011. Derivation of a Reference Shear-Wave Velocity model from Empirical Site Amplification. BSSA, 101, no. 1, pp. 258-274

Poggi, V., B. Edwards and D. Fäh, 2012. The quarter-wavelength average velocity: a review of some past and recent application developments. 15th WCEE, Lisbon 2012.

Poggi, V., and D. Fäh, 2010. Estimating Rayleigh wave particle motion from three component array analysis of ambient vibrations. GJI, 180, no. 1, 251-267.

Redpath, B. B., 1973. Seismic refraction exploration for engineering site investigations: National Technical Information Service, Technical Report E-73-4.

Roesset, J. (1970). Fundamentals of soil amplification. In Hansen, R. J., editor, Seismic Design for Nuclear Power Plants, pages 183–244. M.I.T. Press, Cambridge, Mass.

Schmelzbach C., D. Sollberger, S. A. Greenhalgh, H. Horstmeyer, H. Maurer and J.O.A. Robertsson, 2016. 9C seismic data acquisition for near-surface applications: recording, wavefrom reciprocity and 4C rotation. 78th EAGE conference and exhibition. Extended abstract WS04 B03

SIA, 2014. SIA 261 Einwirkungen auf Tragwerke. Société Suisse des ingénieurs at des architectes, Zurich, Switzerland.

Socco, L.V., and C. Strobbia, 2004. Surface-wave method for near-surface characterization: a tutorial: Near Surface Geophysics, 2, no. 4, 165-185.

Socco, L.V., D. Boiero, S. Foti, and R. Wisen, 2009. Laterally constrained inversion of ground roll from seismic reflection records: Geophysics, 74, no. 6, G35-G45.

Sollberger D., C. Schmelzbach, C. Van Renterghem, J. O. Robertsson and S. A- Greenhalgh, 2016. Single-component elastic wavefield separation at the free surface using source- and receiver-side gradients. SEG International Exposition and 86th annual meeting, 2268 – 2273.

Swisstopo, Service géologique national, 2011. Atlas géologiques de la Suisse 1:25000 : LK 1048 feuille de Rheinfelden.

Swisstopo, Service géologique national, 2019. Digital bedrock elevation model in the Molasse Basin and the larger Alpine valleys. https://shop.swisstopo.admin.ch/en/products/geological_models/bedrock_elevation